

Interfacial electrostatic interaction-enhanced photomultiplication for ultra-high external quantum efficiency of organic photodiodes

Juhee Kim

Pohang University of Science & Technology (POSTECH)

Mingyun Kang

Daegu Gyeongbuk Institute of Science & Technology (DGIST)

Sangjun Lee

Pohang University of Science & Technology (POSTECH)

Chan So

Pohang University of Science & Technology (POSTECH)

Dae Sung Chung (✉ dchung@postech.ac.kr)

Pohang University of Science & Technology (POSTECH) <https://orcid.org/0000-0003-1313-8298>

Article

Keywords: Electric Double Layer, Metal-semiconductor Schottky Interface, Drift-diffusion Approximation of Charge Carriers, Pixelated Prototype Image Sensor

Posted Date: January 29th, 2021

DOI: <https://doi.org/10.21203/rs.3.rs-133471/v1>

License:  This work is licensed under a Creative Commons Attribution 4.0 International License.

[Read Full License](#)

Interfacial electrostatic interaction-enhanced photomultiplication for ultra-high external quantum efficiency of organic photodiodes

Juhee Kim^a, Mingyun Kang^b, Sangjun Lee^a, Chan So^a, and Dae Sung Chung^{a,*}

^aDepartment of Chemical Engineering, Pohang University of Science and Technology (POSTECH), Pohang 37673, Republic of Korea

^bDepartment of Energy Science and Engineering, Daegu Gyeongbuk Institute of Science and Technology (DGIST), Daegu 42988, Republic of Korea

*Correspondence: dchung@postech.ac.kr

Abstract

A photomultiplication-type organic photodiode (PM-OPD), where an electric double layer (EDL) is strategically embedded, is demonstrated with an exceptionally high external quantum efficiency (EQE) of 2,210,000%, responsivity of 11,200 A W⁻¹, specific detectivity of 2.82 × 10¹⁴ Jones, and gain-bandwidth product of 1.92 × 10⁷ Hz as well as high reproducibility. A metal-semiconductor Schottky interface consisting of an EDL enables the stabilization of trapped electron states within the acceptor domains of the photoactive layer by electrostatic interactions, boosting the PM-OPD gain generation. The effects of the EDL on the energetics of trapped electron states are confirmed by numerical simulations based on the drift-diffusion approximation of charge carriers. The feasibility of the fabricated high-EQE PM-OPD is demonstrated *via* a pixelated prototype image sensor. We believe that this new OPD platform opens up the possibility for the ultra-high-sensitivity organic image sensors, while maintaining the advantageous properties of organics.

Introduction

Recently, research regarding photomultiplication-type organic photodiodes (PM-OPDs) with external quantum efficiencies (EQEs) exceeding 100% have been actively conducted^{1,2,3,4,5,6,7,8,9,10}. Because the main application fields of OPDs are expanding not only to cameras, but also to finger/vein/iris recognition sensors and bio-signal sensors, which are operated primarily by weak light sources, PM-OPD can be a promising candidate for the commercialization of OPDs based on their self-signal amplification behavior. The high EQE of PM-OPDs is a result of photoconductive gain generation, where the gain is an index describing the number of conducting charges that can be induced by one generated photon. In the classical theory, the photoconductive gain can be expressed as:

$$G = \frac{\tau_r}{\tau_{\text{transit}}} , \quad (1)$$

where τ_r is the minority carrier recombination lifetime, and τ_{transit} is the carrier transit time^{11,12}. This theory is related to intrinsic gain generation and explains that a transit time shorter than the recombination time allows the photogenerated carriers to circulate within the circuit multiple times, generating gain. More recently reported alternative theory predicts that the high gain observed in the experiments can originate from other external effects such as defects, surface conditions, and surface depletion regions that may localize excess minority carriers, resulting in accumulated excess majority carriers creating gain, or extrinsic gain generation mechanism¹³. In this case, the gain (for a p-type photoconductor) is determined by:

$$G = \frac{\tau_r}{\tau_{\text{transit}}} \left(1 + \frac{\Delta p}{\Delta n} \frac{\mu_p}{\mu_n} \right) , \quad (2)$$

where Δp and Δn are the excess hole and electron densities, respectively, and μ_p and μ_n are the hole and electron mobilities, respectively. Despite the differences in detail, both theories predict that high gain and thus EQE of PM-OPD would be possible by enhancing the trapping

efficiency of minority carriers, which can either prolong the carrier recombination lifetime (intrinsic gain), hole-to-electron mobility ratio, or excess carrier density ratios (extrinsic gain). In conventional p-type PM-OPDs, where the photoactive layer primarily comprises an electron donor material, such as poly(3-hexylthiophene-diyl) (P3HT), with a small number of acceptor molecules (typically 1 wt%), such as [6,6]-phenyl-C₇₁-butyric acid methyl ester (PC₇₁BM), the trapping efficiency of minority carriers or electrons is a function of the energetics of trapped electrons within isolated acceptor molecules used for PM-OPDs because an energetically deep electron trap can suppress the electron detrapping rate. Then one can speculate that employing donor-acceptor combinations with a larger lowest unoccupied molecular orbital (LUMO) offset would result in increased electron trapping efficiency and thus a higher EQE. There have been several reports that introduce various acceptor molecules instead of conventional PC₇₁BM with larger LUMO offset^{7,8,9}; however, a clear correlation between LUMO offset and EQE was not found. In fact, the EQE of high-performance PM-OPDs with various combinations of donor-acceptor molecules remained approximately 100,000%, with a maximum value of 150,000%^{3,6,7,8,9,10}. One possible explanation for this phenomenon is that trapped electrons in localized PC₇₁BM can find various energetically more favorable escape routes other than LUMO offset, such as structural defects or chemical defects, through which trapped electrons can reach the transport level of the donor polymer. This implies that the electron trapping efficiency cannot be significantly improved in a bimolecular donor-acceptor system without external force.

In this study, a new device architecture for extremely high-performance PM-OPDs by introducing an electric double layer (EDL) adjacent to the photoactive layer of a PM-OPD is presented, such that strong electrostatic interactions can occur between intentionally introduced positively charged interfacial molecules and trapped electrons within the acceptor molecules, which can significantly increase the trapping efficiency. A polymer electrolyte, poly(9,9-bis(3'-

(N,N-dimethyl)-N-ethylammonium-propyl-2,7-fluorene)-alt-2,7-(9,9-dioctylfluorene))dibromide (PFN-Br) was introduced as a work-function-modifying layer of indium tin oxide (ITO). It was revealed that PFN-Br not only reduced the work function of ITO to achieve effective Schottky junctions with P3HT, but also efficiently enhance the trapping efficiency, which can be ascribed to electrostatic interactions between the positively charged quaternary ammonium groups and trapped electrons within the isolated PC₇₁BM domains. In addition, preferential and sequential alignments of each counterion (bromide anion), cation and hydrophobic polymer backbone along the vertical direction allowed a highly ordered face-on structure of the upper-deposited P3HT, thereby reducing the defect states within the P3HT crystalline domains and thus enabling additional stabilization of trapped electron states. Drift-diffusion simulation clearly shows the formation of deeper effective trap states owing to the synergetic contributions of the introduced EDL. Several additional experiments with various EDLs were conducted to prove the operating mechanism of the suggested PM-OPD with an unprecedentedly high EQE of 2,210,000%. In the last part, a demonstration of a prototype ultra-sensitive organic image sensor is provided, which is especially advantageous against weak illumination.

Results

The effects of electrostatic interactions on PM-OPDs

Figure 1a shows the device structure suggested in this study. The photoactive layer consists of a P3HT:PC₇₁BM (100:1, w/w) bulk heterojunction, which is typical for PM-OPDs where PC₇₁BM is localized within the P3HT matrix without forming electron percolation pathways. PFN-Br was deposited onto pre-cleaned hydrophilic ITO substrates by using methanol/isopropanol (2:1, v/v) as a processing solvent. Considering the protic solvent nature of methanol and its solvation ability for halide ions¹⁴, it is assumed that the bromide anions can be preferentially adsorbed onto the high-energy ITO surface. Subsequently, a solid-state EDL layer would be formed by the upper deposition of the PFN backbone with electrostatic interactions between the pre-adsorbed bromide anions and quaternary ammonium cations^{15,16,17}. This can be confirmed *via* ultraviolet photoelectron spectroscopy (UPS) measurements for both bare ITO and ITO/PFN-Br surfaces, as shown in Supplementary Fig. 1. An apparent shift in the secondary cut-off region of the UPS spectrum to a higher binding energy was observed in the ITO/PFN-Br surface compared with the bare ITO surface. Such a significant shift in the work function (~0.6 eV) implies the sequential adsorption of bromide anions followed by quaternary ammonium cations onto the ITO surface; therefore, permanent electric dipoles pointing outward from the ITO surface were formed, as reported previously^{15,16,17}. Nevertheless, considering the rotational freedom of the polymer backbone and the operating bias of the PM-OPD, which provide a positive bias to the ITO side, molecular reorientation or ion migration enable the partial exposure of quaternary ammonium cations to the uppermost surface^{18,19}, as illustrated in Fig. 1b. The operation mechanism of a typical PM-OPD can be summarized as follows. Photogenerated and separated electrons are trapped by localized PC₇₁BM (PC₇₁BM content is 1 wt%) domains, and holes have unrestricted transit to the counter electrode by the

applied bias. The trapped electrons near the ITO interface accelerate the additional hole injection from the ITO electrode *via* band bending such that the Schottky barrier can be overcome and injected holes transit to the electrode until electrons are detrapped and recombine with free holes, thereby generating a gain^{2,5}. In other words, the PM-OPD operates based on two key mechanisms: 1) a trapped electron-assisted photoconductive gain generation and 2) a trapped electron-assisted band bending of the Schottky junction to enable hole injection from ITO to the photoactive layer. Therefore, the trapped electron states must be stable to achieve an efficient gain generation. In this context, it is speculated that surface-exposed quaternary ammonium cations can stabilize the trapped electron states within PC₇₁BM *via* electrostatic interactions, as schematically shown in Fig. 1c.

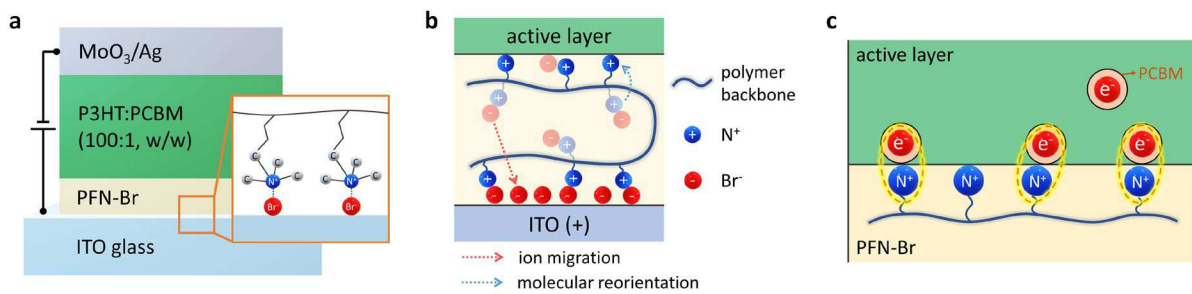


Fig. 1 EDL consisting of polymer electrolyte. **a**, Schematic of the suggested PM-OPD structure. Inset: symbolized chemical structure of bromide anions and quaternary ammonium cations in PFN-Br layer adsorbed onto the surface of ITO. **b**, Illustration of the ion migration or molecular reorientation that occurs in the PFN-Br layer under an external reverse bias. The exposure of quaternary ammonium cations to the interface with the photoactive layer occurs with the movement of bromide anions toward the ITO and the rotational freedom of the polymer backbone. **c**, Schematic description of the interfacial electrostatic interactions between interface-exposed quaternary ammonium cations and trapped electrons near the PFN-Br/photoactive layer interface.

Figure 2a shows the EQE spectra of the optimized PM-OPD under various bias conditions. An unprecedentedly high EQE of 2,210,000% was observed when a reverse bias of 15 V was

applied with a maximum ever reported responsivity of 11,200 A W⁻¹ (Supplementary Fig. 2). The corresponding J - V characteristics are summarized in Supplementary Fig. 3. To date, the highest EQE of PM-OPD was ~150,000% and most other works also remained near ~100,000%^{3,6,7,8,9,10}. The observed EQE in this work which is at least 10-times higher than previous results should be attributed to the dramatically different electron trapping mechanism. At this stage, it is argued that electrostatic interactions between the cations of PFN-Br and trapped electrons at the PFN-Br/P3HT:PC₇₁BM interface enabled such a high EQE. As explained above, the EQE of PM-OPD is primarily determined by the electron trapping efficiency and the flux of electrons emitted from the traps *via* thermally activated excitation, or electron detrapping flux, can be described by

$$J = n_t \frac{1}{\tau_d} \exp\left(-\frac{\Delta E}{kT}\right), \quad (3)$$

where n_t is the density of the filled electron traps, τ_d is the electron detrapping time constant, and ΔE is the effective electron trap energy²⁰. Because the Coulombic attractive interaction energy between a single positive charge and an electron with 1 nm displacement can be as high as several hundreds of milli-electron volts (Supplementary Fig. 4), it is speculated that the detrapping rate of electrons can be significantly suppressed by interfacial electrostatic interactions because of the increased ΔE (based on Equation (3)). In reality, the positive charge encountered by a trapped electron may not be +1, which can result in a lower attractive interaction energy than that suggested in Supplementary Fig. 4. For comparison, polyethyleneimine ethoxylated (PEIE), a non-ionic polymer electrolyte, was introduced as an alternative work-function-modifying layer of ITO, and the same PM-OPD was constructed using PEIE instead of PFN-Br. The UPS spectrum of ITO/PEIE is shown in Supplementary Fig. 5a, which shows that PEIE also effectively functioned as a work function modifier of the ITO surface by ~1 eV. However, the PM-OPD with PEIE yielded a significantly lower EQE

with a maximum of only 62,800%, which is more than 30-times lower than that of PFN–Br, implying that the ionic nature of PFN–Br is crucial for enhancing the EQE of PM-OPD (Supplementary Fig. 5). Despite such a high EQE, the PM-OPD with PFN–Br maintained low dark currents of 1.30×10^{-7} and 4.27×10^{-7} A cm⁻² at -0.1 and -1 V, respectively, owing to the well-defined Schottky junction, which efficiently prevents charge injection under dark conditions. Accordingly, the noise spectra indicated a reasonably low noise-equivalent power (NEP) of 9.94×10^{-16} W Hz^{-0.5} at -15 V as shown in Supplementary Fig. 6. Using the NEP values extracted at each bias condition, the specific detectivity (D^*) was calculated, as displayed in Fig. 2b. An exceptionally high peak D^* of 2.82×10^{14} Jones was measured; it is the highest reported D^* value in visible-detecting OPDs hitherto, primarily owing to the high EQE and responsivity. With the NEP as the lowest measurable light power, the linear dynamic range (LDR) of the PM-OPD was measured, as shown in Supplementary Fig. 7, where ~200 dB of LDR was recorded under various bias conditions. In addition, to confirm that the unprecedentedly high EQE of the suggested PM-OPD platform is reliable, device-to-device reproducibility was tested by measuring OPD performance of 25 independently fabricated PM-OPDs with PFN–Br. The EQE values measured from these PM-OPDs are summarized in Fig. 2c. Of the 25 PM-OPDs, 20 devices showed an EQE of over 1,500,000% with an average EQE of 1,979,000%, implying that the suggested PM-OPD platform is sufficiently reliable.

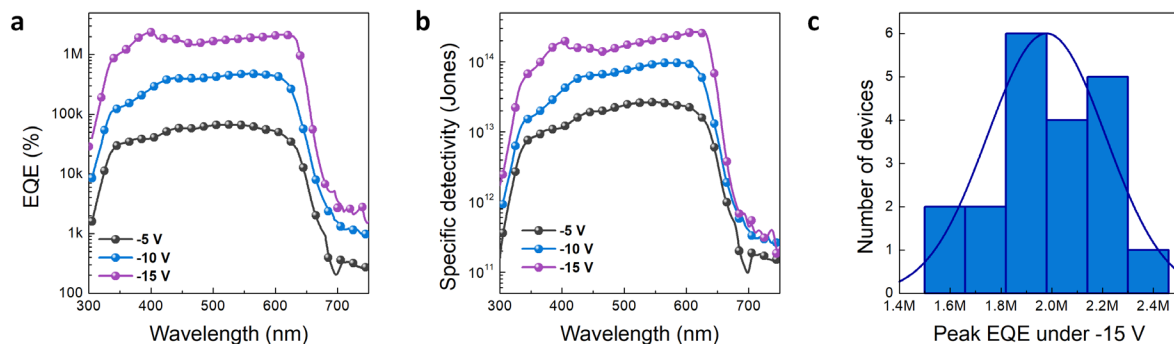


Fig. 2 Effects of interfacial electrostatic interactions on PM-OPD performances. **a,b** EQE (a) and specific detectivity (b) spectra of PM-OPD with PFN–Br under various reverse biases

showing peak values of 2,214,000% and 2.82×10^{14} Jones, respectively. **c** Statistical summary of the EQE vales of 20 independent PM-OPDs with PFN-Br.

Microstructural analyses

Another synergetic contribution of using PFN-Br for the formation of EDL can be found from the morphological improvement of the upper-deposited photoactive layer. In previous studies, although several combinations of donor-acceptor materials were tested, only a similar level of EQE was observed despite the different LUMO offsets, which may be ascribed to the imperfect crystalline ordering of donor polymer semiconductors, resulting in trapped electrons within localized PC₇₁BM to escape *via* energetically more favorable interfacial defect states present in the less ordered region of polymer semiconductors. In this regard, the more ordered and less structural defect morphology of polymer semiconductors can also be advantageous for suppressing electron detrapping and thus increasing the gain. Based on the Fowkes method, the surface energies of three interlayers (PEDOT:PSS, which is most widely used for PM-OPD, PEIE, which is introduced as another interfacial dipole layer, and PFN-Br) and P3HT were measured using a sessile drop of water and diiodomethane, as shown in Supplementary Fig. 8. The contact angles and surface energies obtained are summarized in Supplementary Table 1; making it clear that PEDOT:PSS and PEIE rendered relatively more hydrophilic surfaces with a surface energy of 71.32 and 70.97 mJ m⁻², respectively, whereas the PFN-Br resulted in a relatively less hydrophilic surface with a surface energy of 45.35 mJ m⁻². Because the P3HT layer surface energy was obtained as low as 23.09 mJ m⁻², the cohesive energy between P3HT domains must be lower than the adhesion energy between P3HT and the substrates. In this case, a highly oriented and continuous P3HT crystalline domains can be more easily formed on PFN-Br layer, because of the weaker interaction between P3HT and the substrate. Figure 3a compares two-dimensional grazing incidence X-ray diffraction (2D-GIXD) patterns of

P3HT:PC₇₁BM (100:1, w/w) films deposited onto PEDOT:PSS, PEIE and PFN-Br. The corresponding line-cut profiles along the q_{xy} and q_z axes are displayed in Supplementary Fig. 9. Based on the peak positions of (100) and (010), the d -spacing and π - π stacking distance values of the films were estimated, as summarized in Supplementary Table 2. In all cases, features of simultaneously developed edge-on and face-on orientations were observed, whereas P3HT on PFN-Br showed stronger preferential face-on orientations from the pole figure analysis for the (010) peak of the three films (Fig. 3a), presumably owing to more efficient π - π interactions between the π -conjugated backbones of P3HT and PFN-Br. Paracrystalline disorder (g) which is related to the structural disorder in an imperfect crystal and hence the electrical trap states of a polymer film can be calculated using 2D-GIXD data^{21,22}. The paracrystalline disorder parameter for π - π stacking ($g_{(010)}$), which is an important charge transport direction in diode geometry, can be calculated by using the single peak-width estimation method as follows:

$$g_{(010)} = \sqrt{\frac{\Delta q}{2\pi q_0}}, \quad (4)$$

where Δq is the width of the diffraction peak and q_0 is the center position of the peak. The extracted paracrystalline disorder parameters of P3HT:PC₇₁BM (100:1, w/w) films on PEDOT:PSS, PEIE and PFN-Br were 13.58%, 10.77% and 8.18%, respectively. The 2D-GIXD results clearly confirmed the preferential face-on molecular orientation of the P3HT:PC₇₁BM (100:1, w/w) film on PFN-Br with apparently low paracrystalline disorder, which can result in relatively less amorphous or more ordered regions. To evaluate the actual hole trap state density distribution in the PM-OPDs with PFN-Br or PEDOT:PSS, thermal admittance spectroscopy analysis was conducted, as shown in Fig. 3b. The P3HT:PC₇₁BM (100:1, w/w) film on PFN-Br showed a relatively low hole trap density of 10^{15} - 10^{16} cm⁻³ eV⁻¹ over the entire range, whereas P3HT:PC₇₁BM (100:1, w/w) film on PEDOT:PSS exhibited a higher hole trap density

of 10^{16} – 10^{18} $\text{cm}^{-3} \text{eV}^{-1}$, which is consistent with the 2D-GIXD studies. Although we believe that the electrostatic-driven interfacial contribution is a major source of stabilized electron states for high-EQE PM-OPDs with PFN–Br, the highly ordered morphological feature of the upper-deposited P3HT can also be a reasonable contribution to the observed high gain.

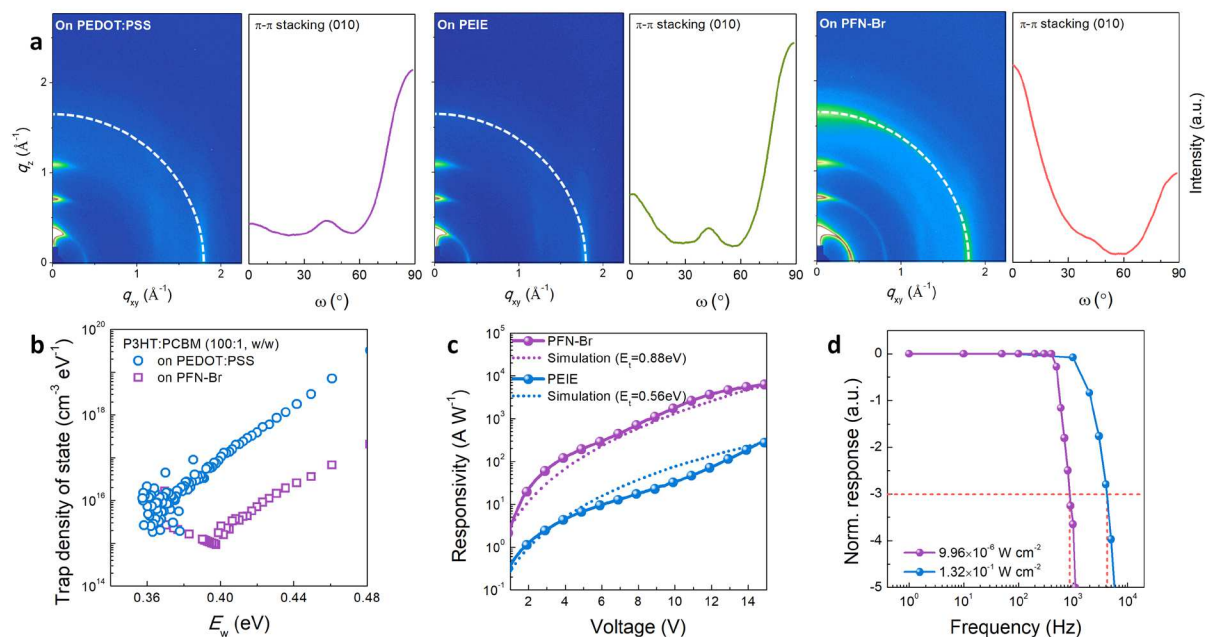


Fig. 3 Morphological effects on electron trapping efficiency. **a**, 2D-GIXD pattern images and pole figure analysis for π - π stacking (white dashed lines) of P3HT:PC₇₁BM (100:1, w/w) films on PEDOT:PSS, PEIE, and PFN-Br layers. **b**, Trap state densities of P3HT:PC₇₁BM (100:1, w/w) films on PEDOT:PSS and PFN-Br layers, obtained using the thermal admittance spectroscopy method. **c**, Experimental (symbol and solid lines) and simulation (dotted lines) R - V curves of PM-OPDs with PFN-Br and PEIE. The used trap energy depths are 0.88 and 0.56 eV, respectively, for the case of PFN-Br and PEIE, respectively. **d**, Bode plot under green (520 nm) light illumination with intensities of $9.96 \mu\text{W cm}^{-2}$ and 0.13 W cm^{-2} , measured under -15 V .

Theoretical interpretation based on numerical simulations

In order to elucidate the effects of the strategically employed EDL on the trapping efficiency, a drift-diffusion simulation was conducted to experimentally fit obtained data and find relevant fitting parameters. To model the injection, transport, generation, and trapping of carriers, the drift-diffusion approximation was used similar to various previous works, and Fluxim software

was used for the actual numerical simulation^{23,24,25,26,27}. For simplicity, a single-level trap state was assumed, as used in various theoretical analyses of charge transport^{28,29}. For boundaries, typical conditions introduced by Schottky were used, which assumes constant electron and hole concentrations at the semiconductor/electrode under an external electric field and illumination^{29,30}. Because electrons are highly localized owing to small contents of PC₇₁BM, hole and electron mobilities were set as 1×10^{-4} and $5 \times 10^{-8} \text{ cm}^2 \text{ V}^{-1} \text{ s}^{-1}$, respectively, which are consistent with hole-only and electron-only space-charge-limited current (SCLC) measurements as summarized in Supplementary Fig. 10. Another important assumption used for the simulation is that the Schottky contact between ITO/PFN-Br and P3HT can be tuned to a pseudo-Ohmic junction because of the nearby trapped electrons under illumination, as suggested in previous studies^{6,7,8}. Therefore, different work function values were used for dark and illumination condition. The optical parameters of each constituting layer were obtained either by our own measurements or from references. All other fitting parameters were carefully set based on several relevant references and our own measurements^{24,26,31}. The details of the simulation parameters are summarized in Supplementary Table 1, which are identical to those of the actual measurements. Figure 3c compares the responsivity versus voltage ($R-V$) relations of PM-OPDs with PFN-Br and PEIE with both experimental and simulated data. In the case of PM-OPD with PFN-Br, trap energy depth of 0.88 eV with respect to the LUMO of P3HT was used, while an apparently smaller trap energy depth of 0.56 eV was enough to reproduce the $R-V$ relation of PM-OPD with PEIE. This indicates that the electrostatic interaction is a direct source of more stabilized trapped electron states, and thus significantly enhances the gain. This simulation also suggests that the design and introduction of a more efficient EDL can yield an even higher EQE.

Other electrolytes for electrostatic interactions

Furthermore, we fabricated a PM-OPD using another ionic polymer electrolyte to prove that the interfacial electrostatic interaction-based strategy for improving the EQE can be universally applied in other ionic work-function-modifying layers. Hence, we introduced a cationic polymer electrolyte, poly{4,8-bis{[(N,N-dimethyl)-N-ethylammonium]propyloxy}benzo[1,2-b:4,5-b]dithiophene-2,6-diyl-alt-3-fluoro-2-[(2-ethylhexyl)carbonyl]thieno[3,4-b]thiophene-4,6-diyl} (PTB7-NBr), as a work-function-modifying layer. As shown in Supplementary Fig. 11a, PTB7-NBr differs from PFN-Br in terms of both the polymer backbone and ionic side chain. The PM-OPD with PTB7-NBr was constructed in the same manner, except that PTB7-NBr was used instead of PFN-Br. The corresponding J - V characteristics and EQE spectra are shown in Supplementary Figs. 11b and c, respectively. The PM-OPD with PTB7-NBr exhibited a high EQE of $\sim 272,600\%$ under a reverse bias of 15 V, which is apparently higher than that of conventional PM-OPDs, demonstrating the validity of the electrostatic interactions between quaternary ammonium cations and trapped electrons. Another example that is expected to yield the same effect is an ionic surfactant. We used cetyltrimethylammonium bromide (CTAB) as a work-function-modifying layer of ITO, and a PM-OPD with CTAB was also constructed in the same manner (Supplementary Fig. 12). The PM-OPD with CTAB also revealed a relatively high EQE of $\sim 356,800\%$ at -15 V, demonstrating the effect of interfacial EDL. The performances of PM-OPDs based on various interlayers are summarized in Table 1.

Table 1. Summary of performances for PM-OPDs based on various interlayers that enable electrostatic interactions, measured under a reverse bias of 15 V.

Structure	Interlayer	EQE (%)	D^* (Jones)	Responsivity (A W^{-1})
Inverted	PFN-Br	2,214,250	2.82×10^{14}	11,236
Inverted	PEIE	62,830	4.18×10^{13}	309

Inverted	PTB7–NBr	272,610	1.31×10^{13}	1,276
Inverted	CTAB	356,790	4.87×10^{13}	1,685
Conventional	PEDOT:PSS	41,980	2.13×10^{13}	206

Response speed of PM-OPDs

One disadvantage of the PM-OPD is its relatively low operational speed, resulting in a significantly limited -3 -dB cut-off frequency^{3,4,32}. According to the traditional intrinsic gain generation mechanism of Equation (1), the gain is directly proportional to the carrier lifetime, and because the carrier lifetime should directly affect the response time of the photodiode, the PM-OPDs often demonstrate slower responses compared with conventional OPDs. The relation between the carrier lifetime and response time of the PM-OPD can be obtained by solving the rate equation for free and trapped holes,

$$\frac{\tau_0}{\tau} = \frac{p_t}{p}, \quad (5)$$

where τ_0 is the response time, and p and p_t are the free and trapped hole carrier densities, respectively. Details regarding the mathematical processes used to attain Equation (5) are available in the Supplementary Information. According to the multiple trap and release model³³, most of free holes can be assumed as trapped holes in the localized trap states, and a small number of holes on the transport bands originating from the trap states by thermal energy can contribute to the electric current. Therefore, it can be assumed that the trapped hole density (p_t) is higher than the free hole density (p), and it can be concluded that the response time of the device should be longer than the carrier lifetime. In this work, the optimized PM-OPD with PFN–Br rendered a reasonably fast response time of 402 μ s, as confirmed by the -3 -dB cut-off frequency of 870 Hz in Fig. 3d. A far shorter lifetime is expected from Equation (5), which

cannot support the observed large gain in this work according to the intrinsic gain generation mechanism described by Equation (1). It is speculated that the observed rather fast temporal response of the high-EQE PM-OPD with PFN-Br can be explained by the extrinsic gain generation mechanism of Equation (2). According to this mechanism, the gain is not only proportional to the carrier lifetime but also proportional to the relative ratio of carrier mobilities and excess charge carrier densities. In other words, a short carrier lifetime does not necessarily result in low gain; rather, the gain generation mechanism is a complex function of carrier lifetime, transit time, defects, and surface conditions. The observed lower defect states of the suggested PM-OPD with PFN-Br (Fig. 3b) presumably enabled optimized combinations of the above-mentioned parameters determining the gain without seriously prolonging the carrier lifetime. Owing to the observed rather fast temporal response of the optimized high-EQE PM-OPD, an unprecedentedly high gain-bandwidth product of 1.92×10^7 Hz was observed when both gain and bandwidth were measured under the same light intensity of 9.96×10^{-6} W cm⁻². Note that the -3-dB cut-off frequency of the optimized PM-OPD with PFN-Br can be increased to 4,170 Hz with a stronger light intensity of 1.32×10^{-1} W cm⁻². This differs significantly from the conventional PM-OPDs structured as ITO/poly(3,4-ethylenedioxythiophene):poly(styrene sulfonate) (PEDOT:PSS)/P3HT:PC₇₁BM (100:1, w/w)/Al, which demonstrates a small bandwidth of less than 10 Hz while exhibiting a high EQE of ~42,000% under a reverse bias of 15 V (Supplementary Fig. 13).

Image sensor demonstration

Considering the exceptionally high EQE of > 2,000,000% and responsivity of > 10,000 A W⁻¹ for the suggested PM-OPD, we prepared prototype organic image sensors consisting of 10 × 10 pixelated PM-OPD arrays. Each pixel feature size was set to 50 μm × 50 μm, defined by

both the top electrode deposited *via* a shadow mask and patterned bottom ITO electrode. For comparison, arrays of conventional BHJ OPDs structured as ITO/PEDOT:PSS/P3HT:PC₇₁BM (50:50, w/w)/Al and conventional PM-OPDs structured as ITO/PEDOT:PSS/P3HT:PC₇₁BM (100:1, w/w)/Al were prepared. Subsequently, we illuminated the prepared OPD arrays with a relatively weak intensity light (520 nm, $6.40 \times 10^{-7} \text{ W cm}^{-2}$ for the BHJ OPD and PFN-Br-based PM-OPD arrays; 600 nm, $5.06 \times 10^{-7} \text{ W cm}^{-2}$ for the PEDOT:PSS-based PM-OPD array) through a star-shaped shadow mask. Next, the photocurrent measured by each pixel was recorded, translated to responsivity, and visualized, as displayed in Fig. 4. All the prepared prototype organic image sensors were successful to read a star-shaped optical signal with high precision. Nonetheless, significantly clearer images could be obtained from arrays of high-EQE PM-OPDs developed in this study, owing to high EQE and thus high responsivity.

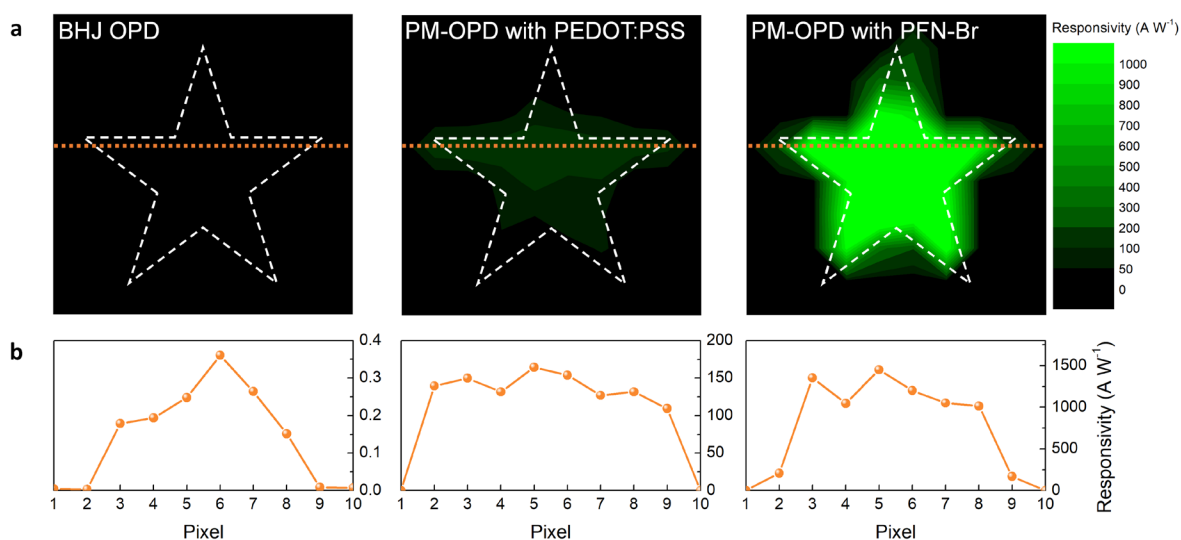


Fig. 4 Demonstration of 10×10 pixelated prototype image sensors. **a**, Two-dimensional contour mapping images of the responsivity distributions for 10×10 pixelated OPD arrays (BHJ OPD, PEDOT:PSS- and PFN-Br-based PM-OPDs). The responsivity distributions were collected when visible light was illuminated on the arrays through a star-shaped shadow mask (white dashed lines). **b**, Line-cut profiles of the corresponding OPD arrays along the indicated orange dotted lines.

Discussion

A new OPD platform for exceptionally high EQE and high responsivity was proposed. Unlike conventional PM-OPDs, where isolated acceptor molecules are solely responsible for the electron trapping mechanism, in this study, we additionally introduced interfacial electrostatic interactions between the surface cations of the PFN–Br interlayer and trapped electrons to realize a more efficient trapping mechanism. In addition, owing to the surface-energetic advantages of PFN–Br, long-range ordered preferential face-on stacking of P3HT was achieved, resulting in a remarkably low paracrystalline disorder, which can also contribute to the stabilized trapped electron states. Such synergetic contributions of PFN–Br EDL enabled an unprecedentedly high EQE of 2,210,000% as well as an unexpectedly high responsivity of $11,200 \text{ A W}^{-1}$ and high specific detectivity exceeding 10^{14} Jones. Numerical simulations based on the drift-diffusion approximation of charge carriers were introduced to explain the effect of the charged interfacial layer on the trapping mechanism. Other interfacial ionic layers which can form solid-state EDL were further tested to verify the effects of electrostatic interaction on stabilizing trapped electron states and thus enhancing gain. The feasibility of the proposed high-EQE PM-OPD platform was tested using fabricated prototype image sensors with $10 \times 10, 50 \times 50$ - μm pixel arrays.

Methods

Materials

PFN–Br was purchased from Ossila and PTB7–NBr was obtained from Lumtec. P3HT and PC₇₁BM were purchased from RIEKE METALS and 1-Material, respectively. PEDOT:PSS (Clevious P VP.AI 4083) aqueous solution was supplied by Heraeus Holding GmbH. CTAB, PEIE, methanol, diiodomethane, Mucosol, acetone, isopropanol, and 1,2-dichlorobenzene

(DCB) were purchased from Sigma-Aldrich. All chemicals were used as received without further purification processes.

Device fabrication

To fabricate PM-OPDs, ITO-patterned glass substrates were cleaned by sequential sonication in a Mucosal solution, distilled water, acetone, and isopropanol, followed by UV-ozone treatment for 30 min. To prepare interlayers of each device, PFN-Br and PTB7-NBr were dissolved in methanol:isopropanol (2:1, v/v) at a concentration of 0.2 mg mL^{-1} , and CTAB was dissolved in distilled water at a concentration of 0.4 mg mL^{-1} . The PEIE solution was diluted in 2-methoxyethanol with a concentration of 0.35–0.4 wt%. All interlayer solutions (PFN-Br, PTB7-NBr, CTAB, PEIE, and PEDOT:PSS) were spin-coated on top of the UV ozone-treated ITO substrates at 5,000 rpm, followed by thermal treatment at $120 \text{ }^{\circ}\text{C}$ for 20 min to evaporate the residual solvent. The P3HT:PC₇₁BM (100:1, w/w) blend was dissolved in DCB at a concentration of 40 mg mL^{-1} . The solutions were stirred at $80 \text{ }^{\circ}\text{C}$ for 24 h, then spin-coated at 1,000 rpm on top of each interlayer, and thermally annealed at $150 \text{ }^{\circ}\text{C}$ for 20 min in a nitrogen-filled glove box. Molybdenum oxide (MoO₃)/Ag or Al electrodes were deposited onto the active layers by thermal evaporation under high vacuum.

Thin film deposition and characterization

The samples for UPS and 2D-GIXD measurements were fabricated with ITO-deposited glass and Si⁺⁺/SiO₂ substrates, respectively, which were deposited with the interlayer solutions as described in the device fabrication section. The UPS measurements were performed with an ESCALAB 250Xi system under high vacuum and an ultraviolet source of He I (21.2 eV) was

used. 2D-GIXD measurements were conducted using PLS-II 3C and 9A beamlines at the Pohang Accelerator Laboratory (PAL) in Korea.

Device characterization

J - V characteristics and EQE spectra were measured using a combination of Keithley 2450 SourceMeter and Oriel Cornerstone 130 1/8 m monochromator, in control of home-made LabView programs. For noise current measurements, a Stanford Research SR830 DSP lock-in amplifier was used in connection with the same SourceMeter. Specific detectivity was calculated using the definition:

$$D^* = \frac{q\lambda\sqrt{A}EQE}{hci_{noise}} , \quad (6)$$

where q is the elementary charge, λ is the wavelength of incident light, A is the photoactive area, EQE is the external quantum efficiency, h is the Planck constant, c is the speed of light, and i_{noise} is the noise current^{30,34,35}. The LDR was measured using two different light sources with various optical filters: monochromatic light (520 nm) from a 300 W Xe arc lamp of the above-mentioned monochromator for light intensities below $4.03 \times 10^{-4} \text{ W cm}^{-2}$, and a laser (520 nm) for light intensities up to $1.32 \times 10^{-1} \text{ W cm}^{-2}$, and calculated using the equation:

$$\text{LDR} = 20\log \frac{P_{\max}}{P_{\text{NEP}}} , \quad (7)$$

where P_{\max} is the maximum value of the detectable power density and P_{NEP} is the power density extracted from NEP^{34,35}. The -3 -dB cut-off frequency and transient photocurrent were measured using a TDS5052 digital phosphor oscilloscope (Tektronix) and an optically filtered laser diode in connection with a Tektronix AFG310 arbitrary function generator. The SCLC analyses were performed with the geometry of ITO/PEDOT:PSS/P3HT:PC₇₁BM (100:1,

w/w)/MoO₃/Ag and ITO/PEIE/P3HT:PC₇₁BM (100:1, w/w)/LiF/Al for hole-only and electron-only devices, respectively. The theoretical fitting was provided by the SCLC equation:

$$J = \frac{9\varepsilon\varepsilon_0\mu(V-V_{bi})^2}{8d^3}, \quad (8)$$

where ε is the relative permittivity of the thin film, ε_0 is the permittivity of free space, μ is the charge carrier mobility, and d is the thin film thickness³⁶.

Acknowledgements

This work was supported by Samsung Research Funding & Incubation Center of Samsung Electronics under Project Number SRFC-TA1803-01.

Author contributions

J. K. and M. K. contributed equally to this work. J. K. and M. K. designed the experimental processes, prepared the samples, and performed the measurements under the overall project supervision of D. S. C. Theoretical studies, such as solving the rate equations and performing the numerical simulations, were conducted by S. L. and C. So. All authors have contributed to the interpretation of the results and the preparation of the manuscript, which was drafted by D. S. C.

Competing interests

The authors declare no competing interests.

References

- [1] Chen, H.-Y., Lo, M. K. F., Yang, G., Monbouquette, H. G. and Yang, Y. Nanoparticle-assisted high photoconductive gain in composites of polymer and fullerene. *Nature Nanotech.* **3**, 543–547 (2008).
- [2] Li, L., Zhang, F., Wang, J., An, Q., Sun, Q., Wang, W., Zhang, J. and Teng, F. Achieving EQE of 16,700% in P3HT:PC₇₁BM based photodetectors by trap-assisted photomultiplication. *Sci. Rep.* **5**, 9181 (2015).
- [3] Zhou, X., Yang, D., Ma, D., Vadim, A., Ahamad, T. and Alshehri, S. M. Ultrahigh gain polymer photodetectors with spectral response from UV to Near-Infrared using ZnO nanoparticles as anode interfacial layer. *Adv. Funct. Mater.* **26**, 6619–6626 (2016).
- [4] Wang, W., Zhang, F., Du, M., Li, L., Zhang, M., Wang, K., Wang, Y., Hu, B., Fang, Y. and Huang, J. Highly narrowband photomultiplication type organic photodetectors. *Nano Lett.* **17**, 1995–2002 (2017).
- [5] Esopi, M. R., Calcagno, M. and Yu, Q. Organic ultraviolet photodetectors exhibiting photomultiplication, low dark current, and high stability. *Adv. Mater. Technol.* **2**, 1700025 (2017).
- [6] Jang, M. S., Yoon, S., Sim, K. M., Cho, J. and Chung, D. S. Spatial confinement of the optical sensitizer to realize a thin film organic photodetector with high detectivity and thermal stability. *J. Phys. Chem. Lett.* **9**, 8–12 (2018).
- [7] Neethipathi, D. K., Ryu, H. S., Jang, M. S., Yoon, S., Sim, K. M., Woo, H. Y. and Chung, D. S. High-performance photomultiplication photodiode with a 70 nm-thick active layer assisted by IDIC as an efficient molecular sensitizer. *ACS Appl. Mater. Interfaces* **11**, 21211–21217 (2019).
- [8] Yoon, S., Lee, G. S., Sim, K. M., Kim, M.-J., Kim, Y.-H. and Chung, D. S. End-group functionalization of non-fullerene acceptors for high external quantum efficiency over 150 000% in photomultiplication type organic photodetectors. *Adv. Funct. Mater.* 2006448 (2020).
- [9] Sim, H. R., Kang, M., Yu, S. H., Nam, G.-H., Lim, B. and Chung, D. S. Design and synthesis of a new non-fullerene acceptor for high-performance photomultiplication-type organic photodiodes. *Adv. Opt. Mater.* 2001836 (2020).
- [10] Wang, W., Zhang, F., Li, L., Zhang, M., An, Q., Wang, J. and Sun, Q. Highly sensitive polymer photodetectors with a broad spectral response range from UV light to the near infrared region. *J. Mater. Chem. C* **3**, 7386–7393 (2015).
- [11] Miao, J. and Zhang, F. Recent progress on photomultiplication type organic photodetectors. *Laser Photonics Rev.* **13**, 1800204 (2019).
- [12] Bibermann, L. M. and Nudelman, S. *Photoelectronic imaging devices: physical processes and methods of analysis* (Plenum press, New York, 1971).
- [13] Dan, Y., Zhao, X., Chen, K. and Mesli, A. A photoconductor intrinsically has no gain. *ACS Photonics* **5**, 4111–4116 (2018).

- [14] Hiraoka, K. and Yamabe, S. Solvation of halide ions with CH₃OH in the gas phase. *Int. J. Mass Spectrom. Ion Proc.* **109**, 133–150 (1991).
- [15] Park, J., Yang, R., Hoven, C. V., Garcia, A., Fischer, D. A., Nguyen, T.-Q., Bazan, G. C. and DeLongchamp, D. M. Structural characterization of conjugated polyelectrolyte electron transport layers by NEXAFS spectroscopy. *Adv. Mater.* **20**, 2491–2496 (2008).
- [16] Choi, H., Park, J. S., Jeong, E., Kim, G.-H., Lee, B. R., Kim, S. O., Song, M. H., Woo, H. Y. and Kim, J. Y. Combination of titanium oxide and a conjugated polyelectrolyte for high-performance inverted-type organic optoelectronic devices. *Adv. Mater.* **23**, 2759–2763 (2011).
- [17] Lee, B. H., Jung, I. H., Woo, H. Y., Shin, H.-K., Kim, G. and Lee, K. Multi-charged conjugated polyelectrolytes as a versatile work function modifier for organic electronic devices. *Adv. Funct. Mater.* **24**, 1100–1108 (2014).
- [18] Fang, J., Wallikewitz, B. H., Gao, F., Tu, G., Müller, C., Pace, G., Friend, R. H. and Huck, W. T. S. Conjugated zwitterionic polyelectrolyte as the charge injection layer for high-performance polymer light-emitting diodes. *J. Am. Chem. Soc.* **133**, 683–685 (2011).
- [19] Hoven, C. V., Garcia, A., Bazan, G. C. and Nguyen, T.-Q. Recent applications of conjugated polyelectrolytes in optoelectronic devices. *Adv. Mater.* **20**, 3793–3810 (2008).
- [20] Bersuker, G., Sim, J. H., Park, C. S., Young, C. D., Nadkarni, S. V., Choi, R. and Lee, B. H. Mechanism of electron trapping and characteristics of traps in HfO₂ gate stacks. *IEEE Trans Dev. Mat. Reliability* **7**, 138–145 (2007).
- [21] Noriega, R., Rivnay, J., Vandewal, K., Koch, F. P. V., Stingelin, N., Smith, P., Toney, M. F. and Salleo, A. A general relationship between disorder, aggregation and charge transport in conjugated polymers. *Nature Materials* **12**, 1038–1044 (2013).
- [22] Rivnay, J., Noriega, R., Northrup, J. E., Kline, R. J., Toney, M. F. and Salleo, A. Structural origin of gap states in semicrystalline polymers and the implications for charge transport. *Phys. Rev. B* **83**, 121306 (2011).
- [23] Koster, L. J. A., Smits, E. C. P., Mihailetchi, V. D. and Blom, P. W. M. Device model for the operation of polymer/fullerene bulk heterojunction solar cells. *Phys. Rev. B* **72**, 085205 (2005).
- [24] Häusermann, R., Knapp, E., Moos, M., Reinke, N. A., Flatz, T. and Ruhstaller, B. Coupled optoelectronic simulations of organic bulk-heterojunction solar cells: parameter extraction and sensitivity analysis. *J. Appl. Phys.* **106**, 104507 (2009).
- [25] Altazin, S., Clerc, R., Gwoziecki, R., Pananakakis, G., Ghibaudo, G. and Serbutoviez, C. Analytical modeling of organic solar cells and photodiodes. *Appl. Phys. Lett.* **99**, 143301 (2011).
- [26] Daanoun, M., Clerc, R., Flament, B. and Hirsch, L. Physics of trap assisted photomultiplication in vertical organic photoresistors. *J. Appl. Phys.* **127**, 055502 (2020).
- [27] A. G. Fluxim, see <http://www.fluxim.com> for more information about SETFOS: Semiconducting emissive thin film optics simulator software.

- [28] Jung, J. H. and Kim, T. W. The effect of the trap density and depth on the current bistability in organic bistable devices. *J. Appl. Phys.* **110**, 043721 (2011).
- [29] K. Marcin, Daanoune, M., François-Martin, O., Flament, B., Dhez, O., Pankey, A. K., Chambon, S., Clerc, R. and Hirsch, L. Insights into the failure mechanisms of organic photodetectors. *Adv. Electron. Mater.* **4**, 1700526, (2018).
- [30] Neamen, D. A. *Semiconductor physics and devices 3rd edition* (McGraw-Hill, New York, 2003).
- [31] Mihailetchi, V. D., Xie, H., de Boer, B., Koster, J. A. and Bom, P. W. M. Charge transport and photocurrent generation in poly(3-hexylthiophene):methanofullerene bulk-heterojunction solar cells. *Adv. Funct. Mater.* **16**, 699–708 (2006).
- [32] Kim, D. Y., Ryu, J., Manders, J., Lee, J. and So, F. Air-stable, solution-processed oxide p-n heterojunction ultraviolet photodetector. *ACS Appl. Mater. Interfaces* **6**, 1370–1374 (2014).
- [33] Lee, E., Ko, J., Lim, K.-H., Kim, K., Park, S. Y., Myoung, J. M. and Kim, Y. S. Gate capacitance-dependent field-effect mobility in solution-processed oxide semiconductor thin-film transistors. *Adv. Funct. Mater.* **24**, 4689–4697 (2014).
- [34] Jansen-van Vuuren, R. D., Armin, A., Pandey, A. K., Burn, P. L. and Meredith, P. Organic photodiodes: the future of full color detection and image sensing. *Adv. Mater.* **28**, 4766–4802 (2016).
- [35] Yoon, S., Sim, K. M. and Chung, D. S. Prospects of colour selective organic photodiodes. *J. Mater Chem. C* **6**, 13084–13100 (2018).
- [36] Nicalar, H. T., Wetzelaer, G. A. H., Kuik, M., Mronemeijer, A. J., Boer, B. de and Blom, P. W. M. Space-charge-limited hole current in poly(9,9-dioctylfluorene) diodes. *Appl. Phys. Lett.* **96**, 172107 (2010).

Figures

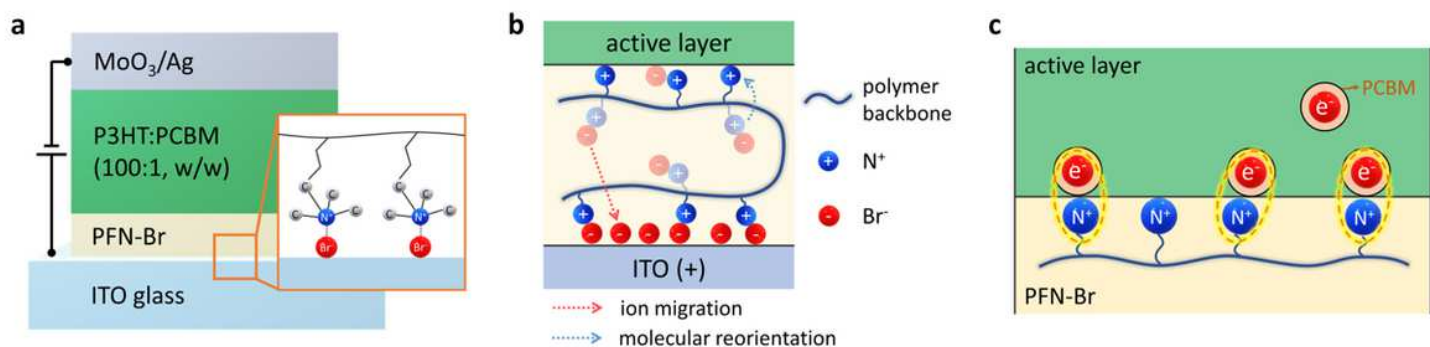


Figure 1

EDL consisting of polymer electrolyte. a, Schematic of the suggested PM-OPD structure. Inset: symbolized chemical structure of bromide anions and quaternary ammonium cations in PFN-Br layer adsorbed onto the surface of ITO. b, Illustration of the ion migration or molecular reorientation that occurs in the PFN-Br layer under an external reverse bias. The exposure of quaternary ammonium cations to the interface with the photoactive layer occurs with the movement of bromide anions toward the ITO and the rotational freedom of the polymer backbone. c, Schematic description of the interfacial electrostatic interactions between interface-exposed quaternary ammonium cations and trapped electrons near the PFN-Br/photoactive layer interface.

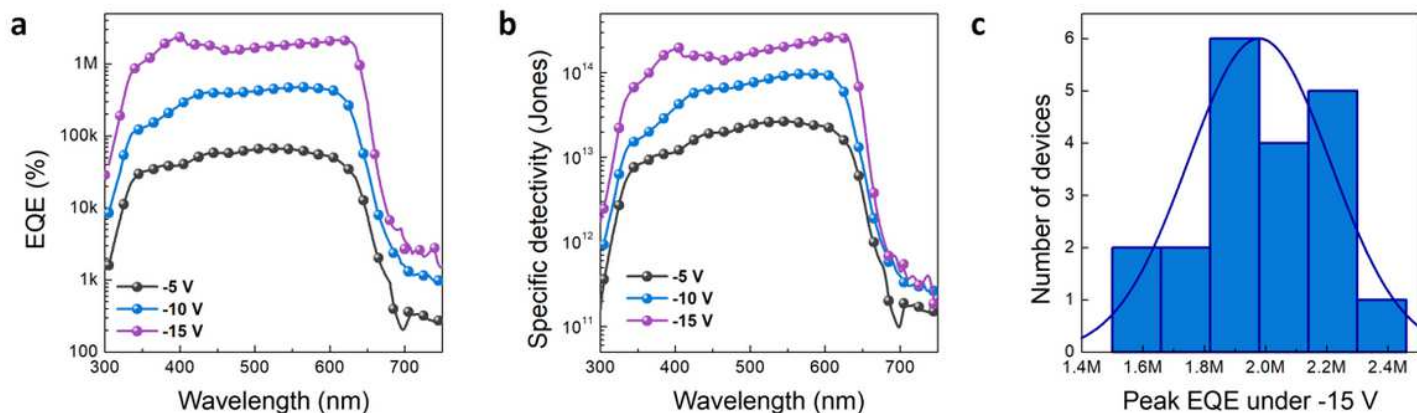


Figure 2

Effects of interfacial electrostatic interactions on PM-OPD performances. a,b EQE (a) and specific detectivity (b) spectra of PM-OPD with PFN-Br under various reverse biases showing peak values of 2,214,000% and 2.82×10^{14} Jones, respectively. c Statistical summary of the EQE values of 20 independent PM-OPDs with PFN-Br.

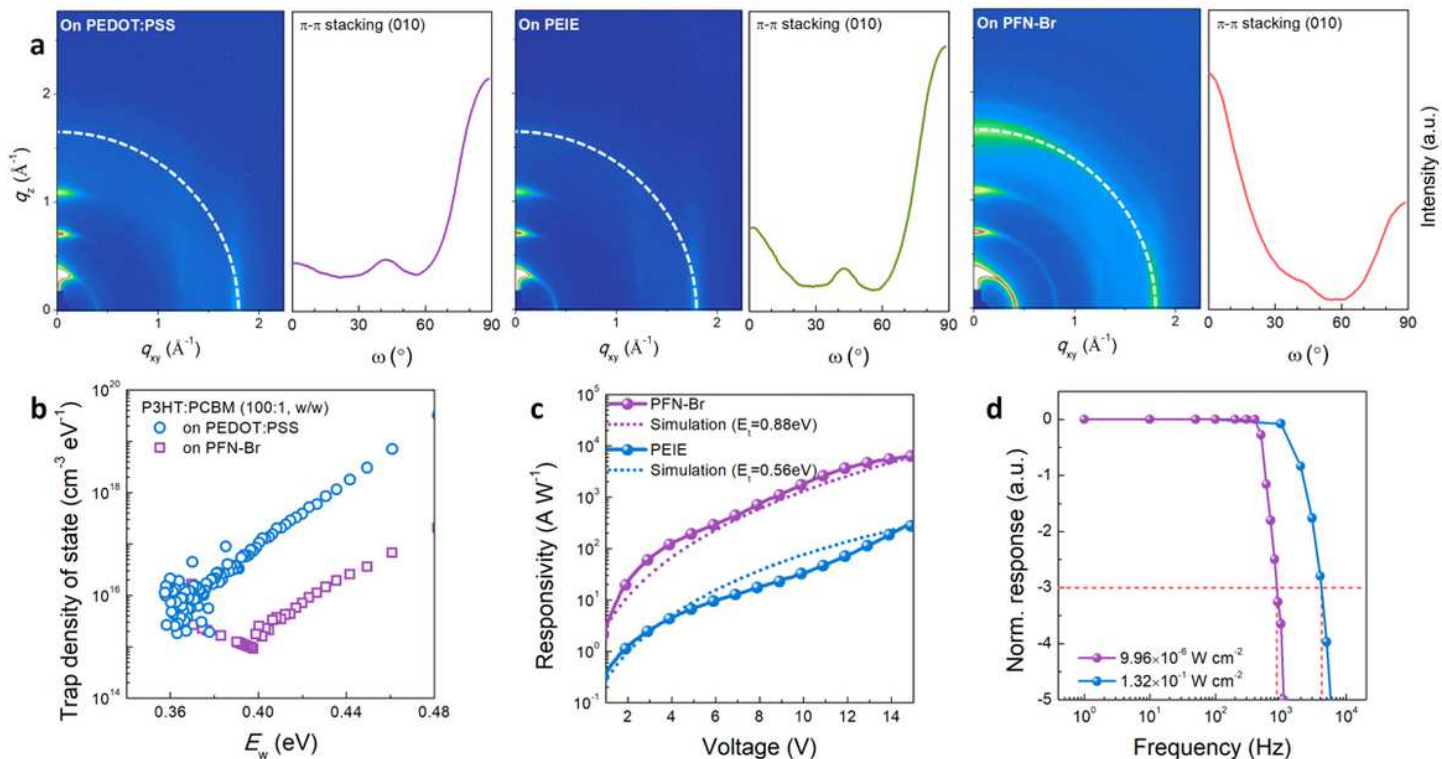


Figure 3

Morphological effects on electron trapping efficiency. a, 2D-GIXD pattern images and pole figure analysis for π - π stacking (white dashed lines) of P3HT:PC71BM (100:1, w/w) films on PEDOT:PSS, PEIE, and PFN-Br layers. b, Trap state densities of P3HT:PC71BM (100:1, w/w) films on PEDOT:PSS and PFN-Br layers, obtained using the thermal admittance spectroscopy method. c, Experimental (symbol and solid lines) and simulation (dotted lines) R-V curves of PM-OPDs with PFN-Br and PEIE. The used trap energy depths are 0.88 and 0.56 eV, respectively, for the case of PFN-Br and PEIE, respectively. d, Bode plot under green (520 nm) light illumination with intensities of $9.96 \mu\text{W cm}^{-2}$ and 0.13 W cm^{-2} , measured under -15 V.

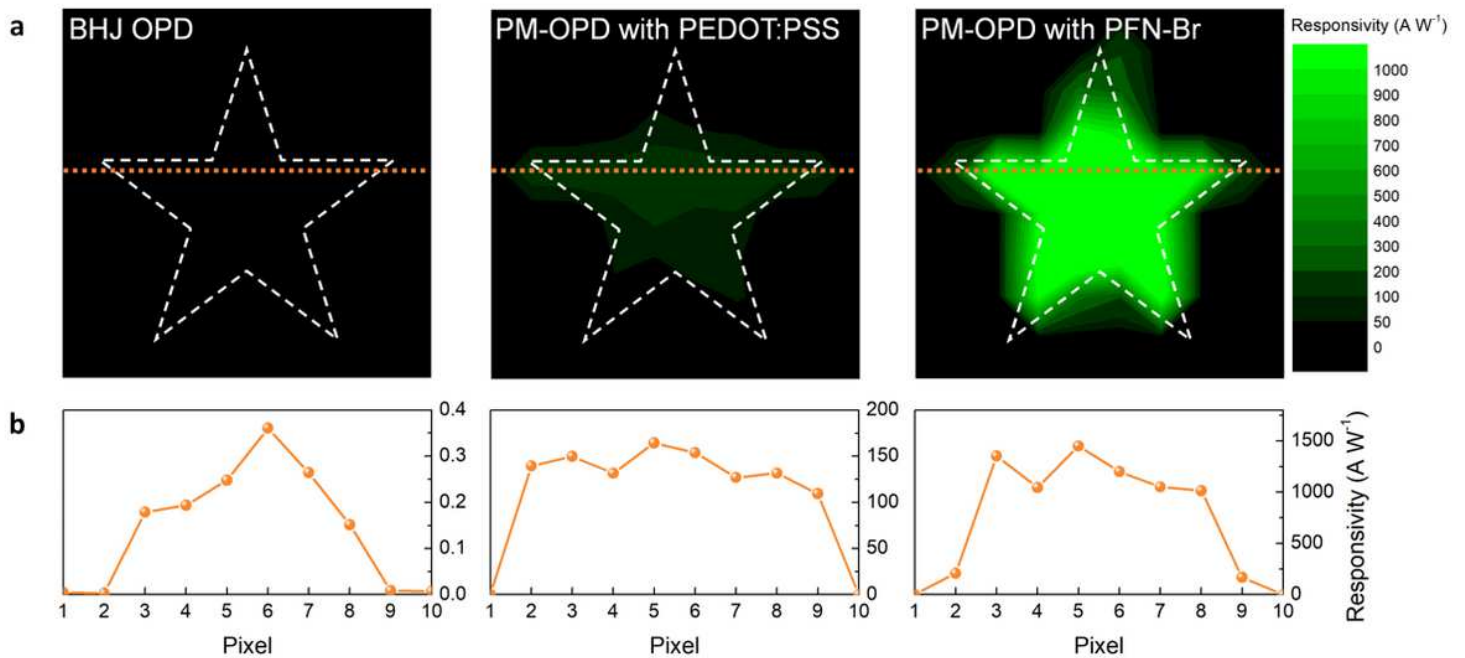


Figure 4

Demonstration of 10×10 pixelated prototype image sensors. a, Two-dimensional contour mapping images of the responsivity distributions for 10×10 pixelated OPD arrays (BHJ OPD, PEDOT:PSS- and PFN-Br-based PM-OPDs). The responsivity distributions were collected when visible light was illuminated on the arrays through a star-shaped shadow mask (white dashed lines). b, Line-cut profiles of the corresponding OPD arrays along the indicated orange dotted lines.

Supplementary Files

This is a list of supplementary files associated with this preprint. Click to download.

- [SupplementaryInformation.pdf](#)